Influence of dissolution on long-term frictional properties of carbonate fault gouge

Hadrien Rattez, F. Disidoro, Jean Sulem, Manolis Veveakis

1   **Influence of dissolution on long-term frictional properties of carbonate fault gouge**

2

3   **H. Rattez[1,4], F. Disidoro[2], J. Sulem[3], M. Veveakis[1]**

4   [1]Duke University, Durham, North Carolina, USA.

5   [2]Politecnico di Torino, Turin, Italy.

6   [3]Laboratoire Navier, Ecole des Ponts ParisTech, UGE, CNRS, Champs-sur-Marne, France.

7   [4]Institute of Mechanics, Materials and Civil Engineering (IMMC), Université Catholique de
8   Louvain, B-1348 Louvain-la-Neuve, Belgium

9   Corresponding author: Hadrien Rattez (hadrien.rattez@duke.edu)

10   **Key Points:**

11   • Velocity stepping experiments have been conducted on a synthetic calcite gouge using an
12   annular shear apparatus to study the effect of the injection of an acid fluid on the long-
13   term frictional properties of the gouge.

14   • The dissolution process affects the particle size distribution of the gouge material and the
15   roughness of the particles.

16   • Experimental results show a decrease toward more negative values of the carbonate
17   gouge Rate and State parameter (a-b) due to dissolution for experiments performed on
18   dry specimens, whereas an increase of (a-b) is observed for wet experiments.

19

20   **Abstract**

21   Velocity stepping experiments have been performed on a simulated calcite gouge using an
22   annular shear apparatus to investigate the effect of dissolution on the frictional properties of a
23   carbonate fault. The tested material was put in contact with hydrochloric acid at different
24   concentration in order to provoke grains dissolution prior to the experiments. Particle size
25   analysis shows that the small grains tend to disappear due to the chemical reaction, whereas the

26 distribution of large grains is not much affected. The dissolution process induces a decrease of
27 the fractal number of the grain size distribution and an increase of the roughness of the particles.
28 The study of the rate-and-state parameter of the materials, which is commonly used to
29 characterize the ability of the fault to generate earthquakes, shows a decrease toward more
30 negative values with dissolution for dry specimens and an increase for wet samples. Moreover, a
31 decrease of the steady state friction coefficient is observed with dissolution for wet samples. This
32 decrease of the friction would promote the triggering of slip along an existing fault after the
33 injection of an acid fluid like in the cases of CO_2 storage or acid gas disposal projects in a
34 carbonate reservoir, but the increase of the rate and state parameter *(a-b)* of saturated specimens
35 implies that the seismogenic potential of faults could potentially be reduced.

36 **1. Introduction**

37 A variety of human activities can modify the stress state or the material properties of
38 underground rocks and, thus, induce potentially a frictional instability at the origin of an
39 earthquake. Human-induced seismicity has been evidenced for a large range of activities (e.g.,
40 (Foulger et al. 2018)). Among them, the most commonly reported anthropogenic activities are
41 mining and water reservoir impoundment, but it can also be caused by hydrofractures, oil and
42 gas extraction, waste water disposal or geothermal projects (Wilson et al. 2017). Human-made
43 seismicity have drastically increased in the U.S. since 2001 from a previous average of 21
44 earthquakes a year to 188 documented in 2011 (Ellsworth 2013). For instance, infrastructures
45 and people in Oklahoma and southern Kansas face potential damages in the next years from
46 induced earthquakes, in a similar level to regions known for their large number of natural
47 earthquakes, like southern California (Schoenball and Ellsworth 2017).

48 Projects like carbon capture and storage, acid gas disposal or enhanced oil recovery involve the
49 injection of a reacting fluid into a reservoir (Khan, Amin, and Madden 2013). Carbon Capture
50 and Storage (CCS) is one of the methods considered to reduce emissions of CO_2 into the
51 atmosphere (Espinoza 2011). The principle is to capture the CO_2 and separate it from other gases
52 in the combustion smoke of large point sources like cement factories or coal-burning power
53 plants. Once extracted, the gas is compressed and transported with a pipeline to injection sites for
54 long term storage. Acid gas disposal is a method used by oil and gas producer to reduce
55 atmospheric emissions of hydrogen sulphide (H_2S). A mixture of hydrogen sulphide and carbon

56 dioxide (by-product of 'sweetening' sour hydrocarbons) is injected into depleted reservoirs or

57 deep saline aquifers (Bachu and Gunter 2004). Enhanced oil recovery, also called tertiary

58 recovery, is a way to improve the extraction of crude oil from reservoir that could not be

59 extracted otherwise (Rubinstein and Mahani 2015). The most common methods are gas or

60 chemical injection that modify the viscosity of the oil and improve its mobility. In these cases,

61 induced seismicity could produce damage to the well or the caprock and deteriorate the sealing

62 of the reservoirs, leading to the failure of the project.

63 A large number of numerical studies have been devoted to study the mechanisms at the origin of

64 induced seismicity and to evaluate the maximum magnitude of the earthquake a project may

65 induce (e.g. Cappa 2012). Most of them consider a hydro-mechanical model and look at the

66 modifications of the stress state at the location of a known fault in a specific site (Baisch et al.

67 2010; Yehya, Yang, and Rice 2018; Mortezaei and Vahedifard 2015; Cappa 2012). In these

68 studies, fluid injection into a reservoir-caprock system bounded by a fault is modelled with

69 different stress state conditions and assuming various permeability conditions. The stress

70 modifications induced by the fluid potentially leading to an earthquake can be computed and the

71 value of the stress drop permits to estimate the magnitude.

72 The injection of an acid fluid does not only change the stress state, but also modifies the

73 properties of the storage medium and can, in particular, affect the mechanical behavior of fault

74 zones. Due to the conditions of stresses, temperature and velocity, many complex couplings are

75 involved in earthquake nucleation and propagation (Rice 2006; Sulem and Famin 2009;

76 Alevizos, Poulet, and Veveakis 2014; Veveakis, Poulet, and Alevizos 2014; Rattez and Veveakis

77 2020). In fault reactivation simulations based on effective stresses modifications, reactivation

78 through a possible decrease in the frictional strength of fault zones is usually not taken into

79 account. However, experimental studies have looked at the influence of physico-chemical

80 interactions on the potential of a fault to create earthquakes (see (Rohmer, Pluymakers, and

81 Renard 2016) for a review in the context of CO_2 storage). The largest impact of the injection of a

82 reacting fluid on the mechanical properties has been observed for carbonate reservoirs (Rohmer,

83 Pluymakers, and Renard 2016), which are potential target formations for CO_2 capture and

84 storage (Michael et al. 2010). Some experiments have looked at the influence of the short term

85 effect of the presence of CO_2-saturated water on the value of the friction coefficient (Samuelson

86 and Spiers 2012; Anne M H Pluymakers et al. 2014) or the velocity dependence of the friction

87 coefficient (Samuelson and Spiers 2012; Rattez, Sulem, and Ghabezloo 2014; A. M.H.
88 Pluymakers, Niemeijer, and Spiers 2016a), which is of primary importance for earthquake
89 nucleation. To our knowledge, the only experimental study on the long-term effect of a contact
90 with an acidic fluid is (Bakker 2017) by modifying the gouge content and the fraction of the
91 different minerals based on chemical calculations.

92 In this work, we perform experiments on analog carbonate fault gouges previously subjected to
93 different degrees of dissolution at different normal stresses. The aim is to assess the effect of
94 long-term exposure to an acidic fluid on frictional properties of a carbonate material (section 3).
95 Carbonate materials are chosen here as many reservoirs and potential sites for injection of CO_2
96 storage or acid gas disposal are carbonate formations (Bjorlykke 2010). The mechanical results
97 obtained from annular shear experiments on dry and wet specimens and microstructural
98 observations are used to infer the micro-physical processes controlling frictional sliding of
99 calcite fault gouges and discuss the potential effect of dissolution on fault's reactivation (section
100 4).

2. Experimental setup
2.1. Materials

103 The material used for the experiments is a carbonate rock powder extracted from the Fergues
104 quarry by the company "les Carrières du Boulonnais" located in the North of France. The
105 powder is produced by crushing of rocks from the quarry and is composed of 99% of calcite
106 ($CaCO_3$) and show traces of quartz (SiO_2), magnesium carbonate ($MgCO_3$), Hematite (Fe_2O_3)
107 and Aluminum Oxide (Al_2O_3). The grain size distribution is obtained using a combination of
108 sieves and hydrometer analysis or laser diffraction. Both methods show similar results and the
109 broad grain size distribution of the material is shown in Figure 1.

110 To study the effect of dissolution, granular samples are placed in a large plastic container with a
111 certain amount of water and then, a solution of hydrochloric acid (mass concentration of 10%) is
112 slowly poured. In the meantime, the solution is stirred with an electric mixer to obtain a uniform
113 dissolution in the sample. Hydrochloric acid is a strong acid and is used here to simulate the
114 long-term effect of dissolution by a weak acid like carbonic acid on the grain size distribution.
115 The reason for using this acid, instead of carbonic acid or other acids, corresponding to the fluid
116 injected in the case of acid gas injection or enhanced oil recovery, is that the kinetics of the

117   chemical reaction is almost instantaneous. The calcium carbonate ($CaCO_3$) is dissolved by the

118   hydrochloric acid (HCl) and the products of reaction are carbon dioxide (CO_2), water (H_2O) and

119   calcium chloride ($CaCl_2$) (Lund et al. 1975). The equation of the chemical reaction is:

$$CaCO_3^{(s)} + 2HCl^{(l)} \rightarrow CaCl_2^{(aq)} + H_2O^{(l)} + CO_2^{(g)}$$
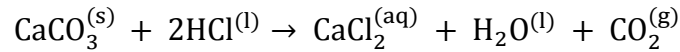
120      $CaCl_2$ is highly soluble (Kirk-Othmer 2004) and the specimens put in contact with the acid are

121   then washed several times with water after the end of the reaction to ensure that this product is

122   removed. The degrees of degradation chosen for this study are 10% and 25% weight percentages

123   of material that is dissolved from the acid during the reaction. The software ChemDigiT is used

124   to calculate the exact quantity of hydrochloric acid required to dissolve the various amounts of

125   materials. Considering that the software provides the amount of pure hydrochloric acid (no

126   dilution with water), while the solution at our disposal had a concentration of 23% in weight

127   (100 g of solution: 23 g of HCl + 77 g of H_2O), we have scaled the provided quantities as

128   function of this concentration. The amount of water initially placed in the container with the rock

129   powder is calculated for the hydrochloric solution to not exceed 10% in weight.

130

131
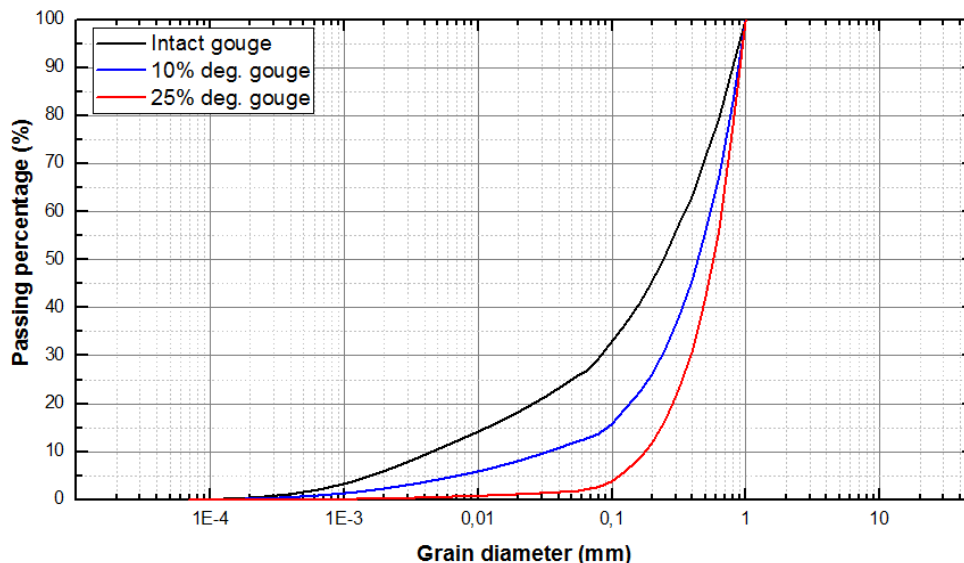
132

133   *Figure 1. Cumulative grain size distribution of the simulated fault materials showing different level of dissolution*

134   The cumulative grain size distributions of the samples for the initial material, after 10% and 25%

135   of dissolution of the total mass are shown in Figure 1. In particular, the higher the degradation,

136   the more the small particles get dissolved. This phenomenon is due to the greater specific surface

137   that small particles offer to the reactive fluid compared to bigger particles.

138   Considering that our tests are carried out on a material that is supposed to simulate a natural fault

139   gouge, one of the most important material properties to be assessed is the fractal dimension of

140   the grain size distribution. The fractal dimension (D) is defined by

141    $N = r^D$, where N is number of particle of diameter r. (Sammis, King, and Biegel 1987)

142   measured the particle distribution of intact gouge samples retrieved from the Lopez Fault in the

143   San Gabriel Mountains of Southern California. The gouge is composed mainly of feldspars,

144   quartz and chlorite, with smaller amounts of calcite and other oxides. The analysis has revealed a

145   remarkable degree of self-similarity for the grain size distribution and the authors have found the

146   fractal dimension to be 1.60 ± 0.11 in two-dimensional cross-section. Thus, the fractal dimension

147   is 2.60 ± 0.11 in a three-dimensional volume as a general result of fractal theory states that the

148   fractal dimension of an isotropic three-dimensional figure is greater by unity than a two-

149   dimensional cross-section of it (Sammis, King, and Biegel 1987). On the basis of the

150   observations, they proposed a new model, called the comminution model, for the mechanical

151   processes that generate fault gouges. Self-similarity results from repeated tensile splitting of

152   grains and that splitting probability depends largely on the relative size of nearest neighbors:

153   during the fragmentation process, the direct contact between two particles of near equal size will

154   result in the tensile breakup of one of the two. In this way, at the end of fragmentation process,

155   the material will have a particle distribution in which particles of the same size are separated

156   from each other. Such a spatial organization repeats itself at each scale, providing a self-similar

157   grain size distribution having a fractal dimension of 2.58, independently of the initial size

158   distribution of the particles. After the development of this model, several authors conducted

159   experiments on natural and simulated fault gouges, showing their tendency to develop a fractal

160   dimension values of about 2.6 supporting the Sammis' theory (Steacy and Sammis 1991; An and

161   Sammis 1994). Moreover, (Biegel, Sammis, and Dieterich 1989) have investigated the frictional

162   properties of gouge presenting fractal dimension of 2.6 and in particular the role of the minimum

163   and maximum grain size. However, (Storti, Billi, and Salvini 2003) have analyzed gouge

164   samples of a carbonate fault in the Apennines, Italy and have shown that for this material the

165   comminution model is not always verified. Fractal dimensions obtained from fault cores varies

166   from 2.61 to 3.49 in strike-slip faults' gouge and between 2.17 to 2.74 in the breccia zones. They

167 recognized the value 2.6 to be a threshold between a first stage of fault gouge formation
168 dominated by particles fragmentation and a second one dominated by particles abrasion in the
169 case of carbonate materials.

170 In Figure 2, the number of particles as a function of the grain diameter is shown for the different
171 level of dissolution of the grains. The value of the fractal number of the simulated gouge that is
172 not dissolved (intact) is in agreement with the comminution theory and this material can,
173 therefore, be considered as a good analog of a gouge material at the first stage of formation. The
174 dissolution induces a decrease of the fractal number from 2.59 to 2.16. This decrease is due to
175 the preferential dissolution of the small particles from the grain size distribution, in the same way
176 that abrasion makes the fractal number increase due to the creation of more small particles. An
177 interesting feature of the effect of dissolution on the particle size distribution is that it induces an
178 increase of the mean grain diameter. It can, thus, affect the prediction of continuum models
179 considering the mean grain size explicitly into the constitutive laws. These class of models are
180 used in particular to regularize the problem of strain localization like Cosserat continua (Rattez,
181 Stefanou, Veveakis, et al. 2018).

182
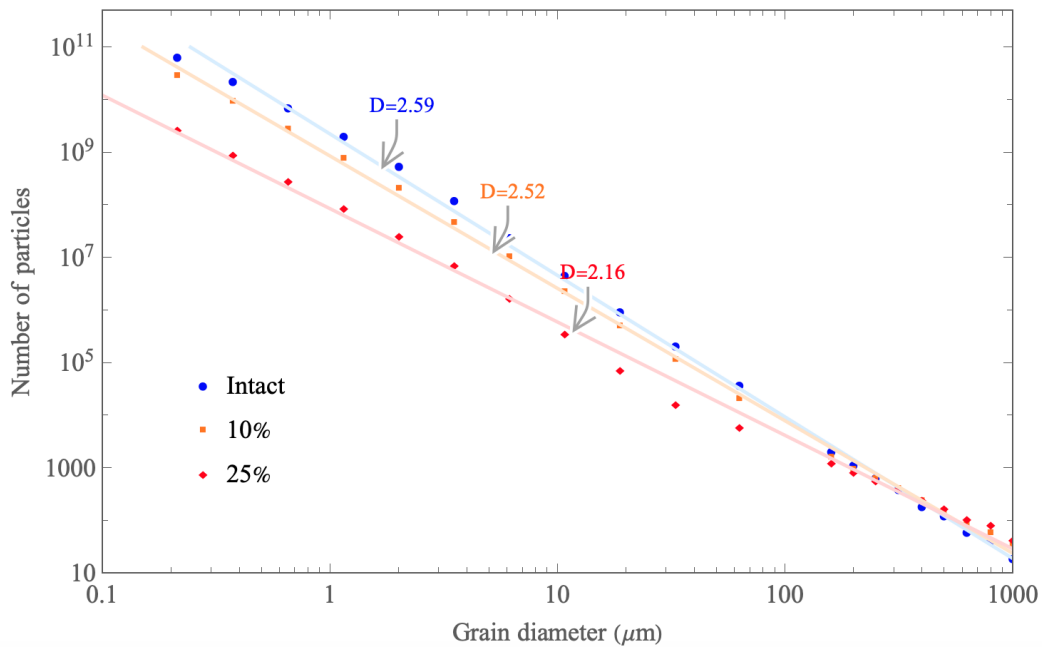
Figure 2. Number of particles as function of the grain diameter for different level of dissolution of the carbonate rock powder.
The points represent the experimental data obtained from sieve and hydrometer analyses. The lines represent an interpolation of
the experimental data using a power law. The fractal number associated D with each distribution is also shown.

2.2. Experimental set-up

7

187 The device used for the mechanical tests is an annular simple shear device called ACSA

188 ("Appareil de Cisaillement Simple Annulaire"), designed in 1993 in the CERMES laboratory of

189 Ecole des Ponts (Unterreiner et al. 1993). It has been used in the context of fault mechanics by

190 (Guillaume Chambon, Schmittbuhl, and Corfdir 2006a, 2006b; Messen, Corfdir, and

191 Schmittbuhl 2013). This device enables to shear the gouge material over large displacements and

192 with samples that are thicker than other experimental devices. This thickness of the samples

193 (10cm) represents an average value of the fault core thickness measured on outcrops of carbonate

194 rocks (Billi 2005; Torabi, Johannessen, and Ellingsen 2019). A schematic view of the machine is

195 shown in Figure 3. We only present here this apparatus briefly. A more detailed description can

196 be obtained from (Guillaume Chambon 2003; Corfdir, Lerat, and Vardoulakis 2004).

197 The internal surface of a ring-shaped sample, which presents a square section of $100*100mm^2$, is

198 sheared by the rotation of a rough steel cylinder. A 15-bit optoelectronic rotation encoder is used

199 to monitor the rotation angle ϕ of the steel cylinder providing a 0.011° resolution. The tangential

200 displacement δ at the inner boundary of the sample is deducted as $\delta = \phi.R_i$ (where R_i is the inner

201 radius of the sample) and is measured with a resolution of $1.92 \ 10^{-5}$ m. The spacing between the

202 vertical triangular striation of the inner interface is 1mm, the same size as the maximum grain

203 diameter of the samples, in order to preclude interfacial slip along the steel-granular boundary

204 (Koval et al. 2011). The outer boundary of the sample is subjected to a constant radial

205 confinement σ_e through a 1.5-mm-thick neoprene jacket and applied using water by a pressure-

206 volume controller (max. press: 2 MPa, vol.: 10^{-3} m^3, resolution: 1 kPa and 1mm^3, accuracy

207 <0.25 per cent). Vertically, the sample is embedded between an upper plate made of duralumin

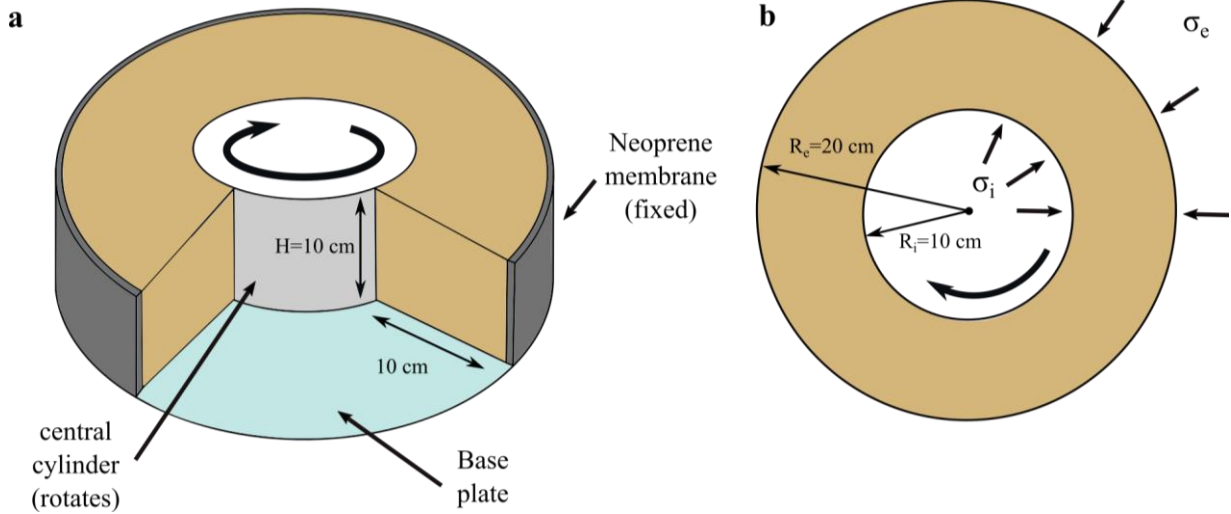208 and a lower plate made of glass.

Figure 3. Schematic view of ACSA: a, Cut away view, b, top view

For a given normal stress, the samples are initially sheared at a constant speed of 33 μm/s for 10 cm, in order to reach the steady-state friction coefficient. Then, the shearing velocity is instantaneously changed every 2 mm of slip to apply different velocity steps. The sequence shown in Table 1 is chosen such that each velocity step is repeated at least twice to better constrain the value of the friction parameters calculated. At the end of this phase, the shear force is unloaded, normal stress is increased and the procedure is repeated as in (Scuderi et al. 2013; Berend A. Verberne et al. 2015). It should be noted that the different normal stresses applied on the sample in this case also correspond to different applied displacements to the sample, which could affect the mechanical behavior.

Stage	1	2	3	4	5	6	7	8	9
Displacement [mm]	100	2	2	2	2	2	2	2	2
Speed [μm/s]	33	10	1.7	10	33	10	1.7	10	33

Table 1. Velocity stepping sequence applied to the sample for a given normal stress.

In Table 2, a list of all the conducted tests with different degrees of dissolution, different stages consisting of various normal stresses and conditions of saturation is presented. The "dry" experiments have been conducted in nominally dry conditions, that is with room atmosphere inside the pore space, while the "wet" experiments are conducted on specimens that are saturated with deaerated water and tested in drained conditions. We note that the samples were saturated in two steps: the water was first injected from the bottom of the specimen until the water level reached the valves located at the top, then the flow through the specimen was maintained until

9

228 half the total volume of pore space of the specimen was expelled at the top, to ensure conditions
229 close to homogeneous saturation.

Degradation	σ_i (MPa)	saturation	Set of data name
none	0.6	dry	Intact0.6
none	1	dry	Intact1
none	1.6	dry	Intact1.6
10%	0.6	dry	10deg0.6
10%	1	dry	10deg1
10%	1.6	dry	10deg1.6
25%	0.6	dry	25deg0.6
25%	1	dry	25deg1
none	0.6	wet	Intact0.6w
none	1	wet	Intact1w
none	1.6	wet	Intact1.6w
10%	0.6	wet	10deg0.6w
10%	1	wet	10deg1w
10%	1.6	wet	10deg1.6w
25%	0.6	wet	25deg0.6w
25%	1	wet	25deg1w
25%	1.6	wet	25deg1.6w

230 Table 2 – List of complete set of phases and experiments

231 **2.3. Data acquisition and processing**

232 The apparent friction coefficient μ of the sample is calculated as the ratio of the applied shear
233 stress τ to the normal stress σ, $\mu = \frac{\tau}{\sigma}$. The shear stress τ can be found converting the applied
234 torque measurements Γ, measured by a torquemeter of 20 N.m accuracy:

$$\tau = \frac{\Gamma/r}{2\pi r H} = \frac{\Gamma}{2\pi r^2 H} \quad \#(1)$$

235 where r and H are respectively the radius and the height of the inner cylinder and are both equal
236 to 10 cm. The normal stress exerted on the inner cylinder is different from the external normal
237 stress applied on the outer boundary of the sample due to the particular geometry of the sample.
238 According to (Guillaume Chambon 2003), simple geometrical considerations indicate that the
239 inner normal stress σ_i should be equal to twice the applied confinement σ_e, since the external
240 radius of the sample is the double of the internal one; moreover, the same authors conducted
241 some experiments equipping both the smooth and the rough cylinder with five stress sensors, and

10

242 they found that normal stress on cylinders' surface was strongly varying at the beginning of the
243 test, but it tended to stabilize after few millimeters of slip toward values very close to the double
244 of external pressure. As the shear band is developing near the inner cylinder, the apparent
245 friction is calculated as:

$$\mu = \frac{\tau}{\sigma_i} = \frac{\Gamma}{2\pi r^2 H} \cdot \frac{1}{2\sigma_e} \#(2)$$

246 **2.4. The Rate-and-State Friction (RSF) law**

247 (Reid 1910) was the first to argue after the 1906 San Francisco earthquake that this phenomenon
248 is not created by the emergence of a new crack in the crust, but rather by the sudden slip along an
249 existing fault. After the beginning of slipping the fault can move aseismically or seismically
250 (Scholz 1998) if a frictional instability is triggered. An empirical law describing the instability
251 along a fault was developed during the eighties by Dieterich and Ruina (Dieterich 1981; Ruina
252 1983). They introduced new state variables that describe a second order effect on the coefficient
253 of friction. These laws are called "Rate and State", because the friction depends on the velocity
254 of slipping (Rate) and a state variable θ, which is interpreted as the average lifespan of a set of
255 grain-to-grain contacts in a frictional system. They describe the evolution of the friction
256 coefficient to changes in sliding motions by the equation:

$$\mu = \mu_0 + a \ln\left(\frac{V}{V_0}\right) + b \ln\left(\frac{V_0\,\theta}{D_c}\right) \#(3)$$

257 μ_0 is a reference friction coefficient, V and V_0 are respectively the actual and reference velocities
258 of the fault. D_c is the critical slip distance representing the slip necessary to renew contacts,
259 associated with the state variable θ (Marone 1998). a and b are empirical parameters. The
260 observed evolution of the state variable can be described by the following equation (Dieterich
261 1979):

$$\frac{d\theta}{dt} = 1 - \frac{v\theta}{D_C} \#(4)$$

262 These empirical laws can capture the repetitive stick-slip failure at the origin of the seismic
263 cycle. A simple system called the spring-slider model, in which the slider follows the rate and
264 state friction laws and the spring represents the elastic surrounding mass of the fault, is usually
265 applied to model seismic slips. The study of the linear stability of that system (Rice and Ruina

266   1983) shows a critical value for the stiffness of the spring k_{cr} (if the inertial terms are
267   negligible). Under this value, the system is unstable and over this value, it is conditionally stable.

$$k_{cr} = \frac{\sigma_N}{D_c}(b - a) \#(5)$$

268   where σ_N is the effective normal stress applied perpendicular to the direction of sliding.
269   The parameter $(a - b)$ is therefore fundamental to determine the stability of a fault modelled
270   with a rate and state friction law, because if it is positive, frictional instability would not nucleate
271   with this model. Moreover, a modification of the value of (a-b) in the velocity-weakening regime
272   modifies the value of the critical stiffness and, if (a-b) becomes more negative (stronger
273   weakening), it can lead to seismic slips for faults that were stable before the modification.

274   The parameter $(a - b)$ can be calculated based on the values of the steady-state friction before
275   and after an instantaneous velocity change. At steady-state $(d\theta/dt = 0)$ and the state evolution
276   law gives $\theta = D_C/v$. So, equation (3) becomes:

$$\mu = \mu_0 + (a - b)\ln\frac{v}{v_0}\#(6)$$

277   To evaluate the friction parameter (a-b), the general long-term strain trend of the apparent
278   friction is removed in order to avoid this factor to influence the (a-b) values. It is typically a
279   softening trend as the one shown in Figure 4. The same procedure was also applied by several
280   studies (Blanpied, Lockner, and Byerlee 1995; Tembe, Lockner, and Wong 2010; Samuelson and
281   Spiers 2012) for velocity stepping experiments.
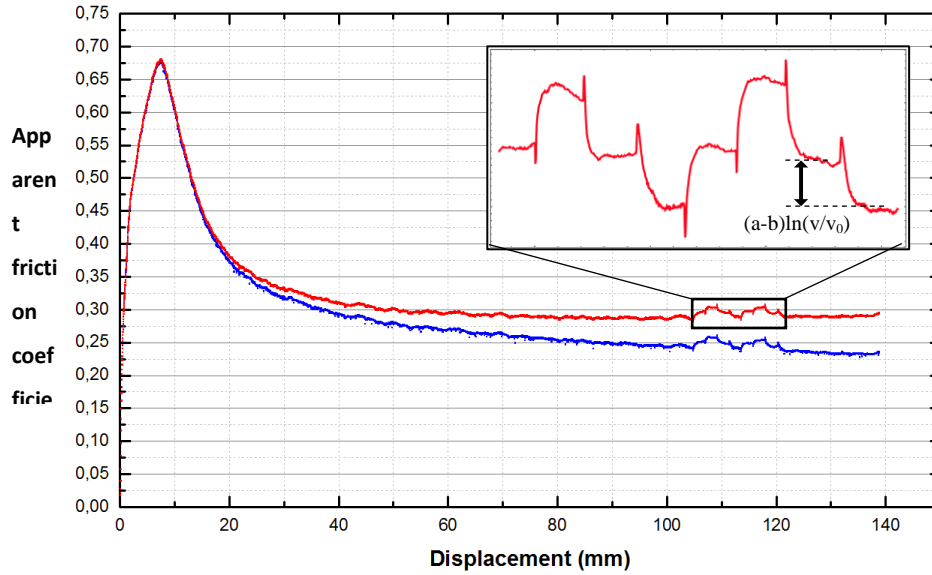
Figure 4. Apparent friction coefficient evolution with displacement: original (blue) vs detrended (red) (intact0.6).

The (*a-b*) value of each velocity step can be obtained from the detrended evolution of the friction coefficient, and in particular, from the value of residual friction before the velocity change and the one obtained once a new steady state is obtained after the change:

$$(a - b) = \frac{\mu_0 - \mu}{\ln(V/V_0)} \#(7)$$

where μ is the coefficient of friction at the end of a step with velocity V, and μ_0 and V_0 are the coefficient of friction and velocity immediately prior to the velocity step.

3. Results

In this section, we describe first the frictional data obtained from the mechanical experiments. The global evolution of the apparent friction as well as the rate and state parameter *(a-b)* are presented together with their evolution with normal stress and dissolution rate. Secondly, the specific surface areas of the samples are assessed by two methods in order to estimate the rugosity of the grains. This analysis is completed with observations obtained using a scanning electron microscope to interpret the different mechanical responses of the samples.

3.1. Mechanical results

An example of the apparent friction coefficient evolution with shear displacement is shown in Figure 4. It exhibits a peak for a value between 0.6 and 0.7 for all dry experiments at 600 kPa of imposed normal stress. The peak is more pronounced for a normal stress of 600 kPa as it is the

13

300   first run applied to the material. This peak is followed by a slip-weakening behavior with a

301   characteristic slip distance of a few centimeters, also observed in the experiments performed on

302   glass beads and quartz sand by (Guillaume Chambon, Schmittbuhl, and Corfdir 2006a). The

303   evolution of the shear stress for all the stages of the experiments is shown in Figure 5 for the

304   different samples. The peak stress is less important for the normal stresses 1 and 1.6 MPa than

305   for 600 kPa due to the multi-stage procedure.

306   We observe through the glass window at the bottom of the sample a strain localization of the

307   deformation next to the inner cylinders. The shear band thickness is on the order of a few

308   millimeters, which corresponds approximately to 10 times the mean grain size, in accordance

309   with results of numerical simulations of continuum models of granular media (Rattez, Stefanou,

310   Sulem, et al. 2018; Rattez, Stefanou, and Sulem 2018). However, digital image correlation needs

311   to be used to observe accurately the evolution of the thickness with increasing displacements as

312   in (G. Chambon et al. 2003) but has not been carried out for this study.

313   The value of the friction μ is not much affected by the dissolution in the dry case (see Figure 5

314   and Table 3), except for the residual friction at 1.6 MPa of normal stress. We can see that for the

315   tests performed under 600 kPa of normal stress, the three peak values are nearly the same

316   (μ=0.63–0.67), as well as the residual values (μ=0.22–0.25). The same happens in the tests under

317   1 MPa of normal stress where the peak is exactly the same and the intact residual value is only a

318   bit higher that the degraded ones (μ=0.20). Finally, the 1.6 MPa run exhibits only a difference in

319   the value of the residual friction. In the wet experiments, the peak values and the residual friction

320   coefficients show a decrease with the dissolution (except the peak stress between the intact and

321   deg10 for the 600 kPa, which can be due to different degrees of initial compaction) for all normal

322   stresses. For the wet experiments, the residual friction decreases from μ=0.27–0.33 for the intact

323   gouge to μ=0.14–0.15 for the gouge dissolved at 25%.

324   Regarding the velocity stepping experiments, the results presented in Figure 6 and Figure 7 show

325   that all of the tests performed in this study, regardless of degradation level and pressure, exhibit a

326   velocity weakening behavior. The *(a-b)* values are falling between -0.003 and -0.018; the only

327   exception is the 25deg0.6dry test (see Table *2* for the denomination of the tests), which exhibits a

328   more negative value of (*a-b*) reaching -0.028.

For dry samples, we can see that deg10 results are situated between intact and deg25 ones (see Figure 6 a, c, e). It means that a larger amount of degradation induces a more pronounced velocity-weakening, and this trend is clear for the tests at 0.6, 1 MPa of normal stress and the velocity steps 10-33 µm/s at 1.6 MPa, but is not visible for the velocity steps 1.7-10 µm/s at 1.6 MPa. For the wet experiments, the opposite effect is observed (see Figure 6 b, d, f), the dissolution of the grains leads to coefficients (a-b) that are less negative, even though we still observe a velocity weakening.
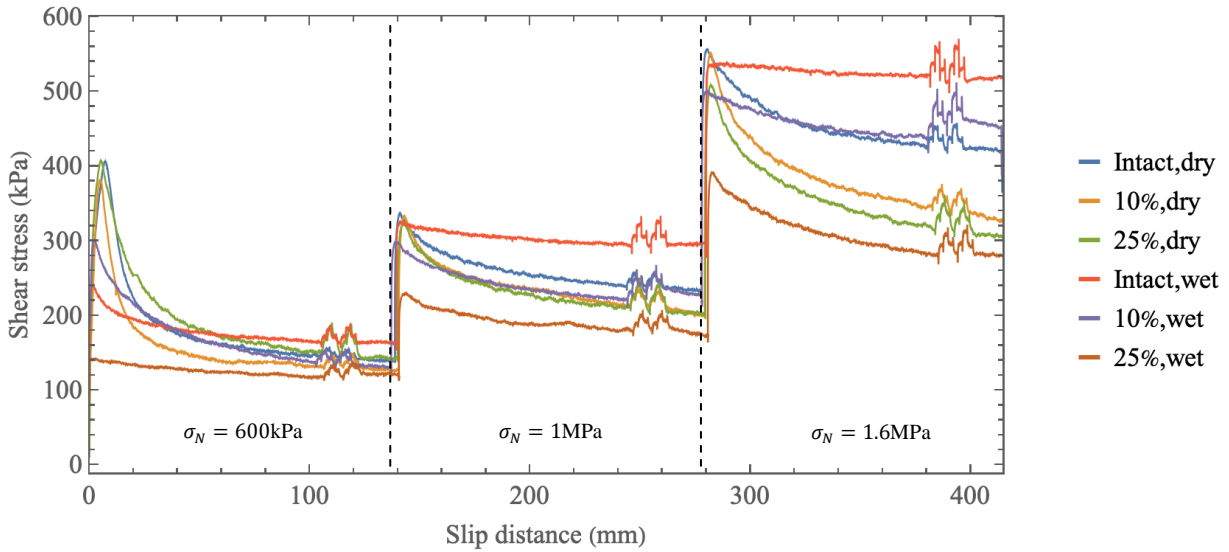
Figure 5. Shear stress as a function of the displacement of the inner cylinder for the different experiments

	0.6 MPa		1 MPa		1.6 MPa	
	peak	residual	peak	residual	peak	residual
intact	0.67	0.24	0.34	0.24	0.35	0.26
dissolution 10%	0.67	0.21	0.33	0.20	0.34	0.21
dissolution 25%	0.64	0.24	0.32	0.20	0.32	0.19
Intact, wet	0.4	0.27	0.33	0.30	0.33	0.33
dissolution 10%, wet	0.5	0.22	0.3	0.23	0.31	0.29
dissolution 25%, wet	0.24	0.15	0.23	0.14	0.24	0.14

Table 3. Values of the residual apparent friction coefficient for different normal stresses and level of dissolution

343 In Figure 7, the values of the friction parameters *(a-b)* are plotted as a function of the normal

344 stress for the different degrees of dissolution and velocity steps. The different values obtained for

345 a velocity step are calculated as an average of the values of the velocity jumps involving the

346 same velocity values (velocity jump 10-33 µm/s: 1-2, 4-5, 5-6, 8-9; velocity jump 1.7-10 µm/s:

347 2-3, 3-4, 6-7, 7-8). For the intact gouge, the rate and state parameter *(a-b)* increase slightly with

348 the normal stress but a more visible dependency on the velocity steps considered is observed.

349 The transition from 10 to 33 µm/s induces more weakening than the transition from 1.7 to 10

350 µm/s. This effect is also observed for the degraded gouge. The dry gouges that underwent 10%

351 and 25% dissolution show a distinct increase of the rate and state parameter *(a-b)* with the

352 normal stress (more pronounced for 25% dissolution). In these tests, the *(a-b)* values get closer to

353 zero when the confinement pressure is increased. For the intact sample, *(a-b)* shows no clear

354 variation with the normal stress. For the wet samples, we also observe a slight increase of *(a-b)*

355 with the normal stress for the intact sample. However, for the samples with 10 and 25%

356 degradation, this increase is only observed for the velocity step 10-33 µm/s and no clear trend is

357 observed for the velocity step 1.7-10 µm/s. It should be noted that the different normal stresses

358 applied here correspond also to larger displacements due to the multi-stage applied to the

359 material, which could affect the evolution of *(a-b)* observed here.

360
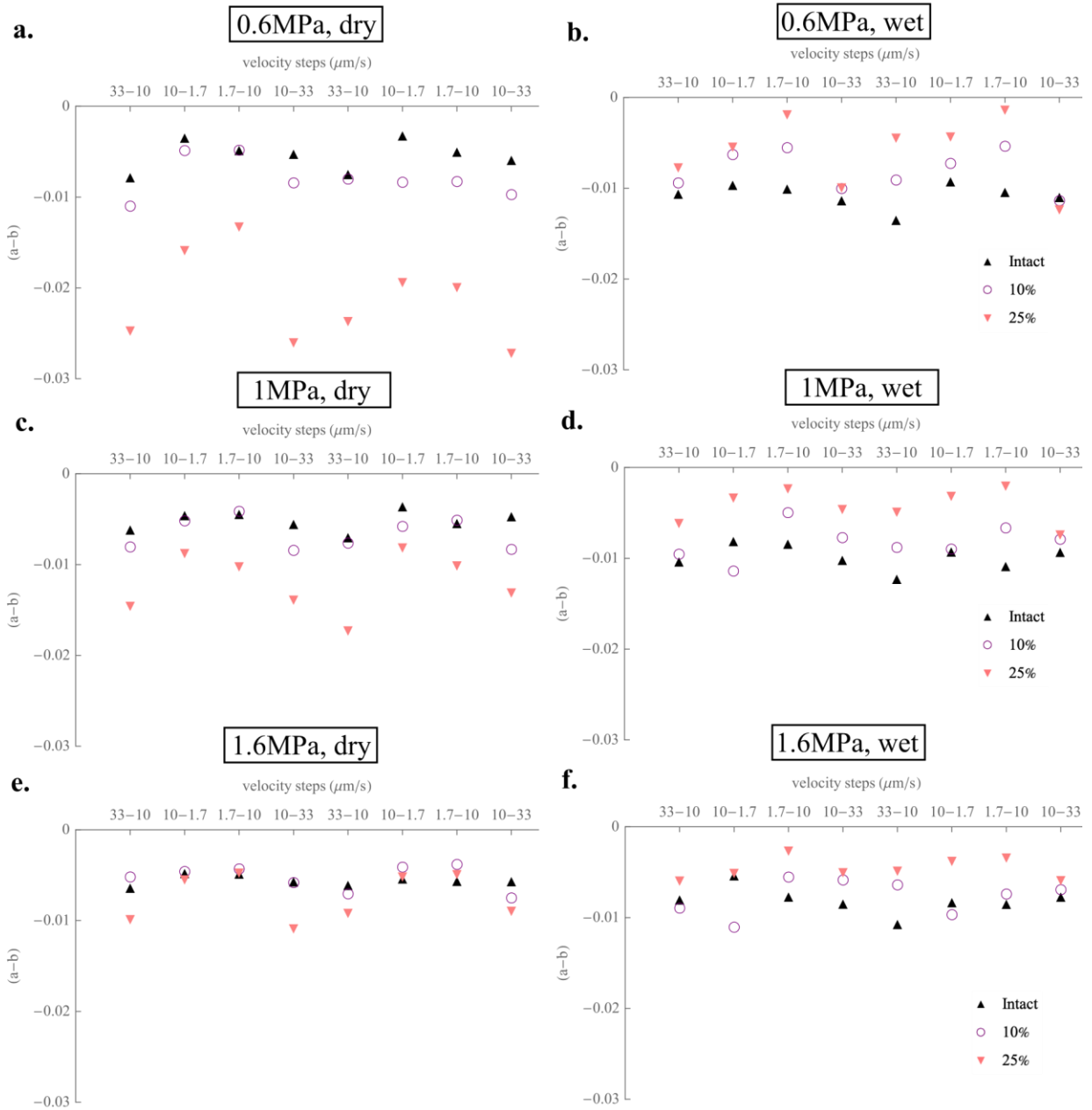
361 *Figure 6. Effect of the dissolution on the rate and state friction parameters (a-b) for the different velocity steps and for different*
362 *normal stress.*
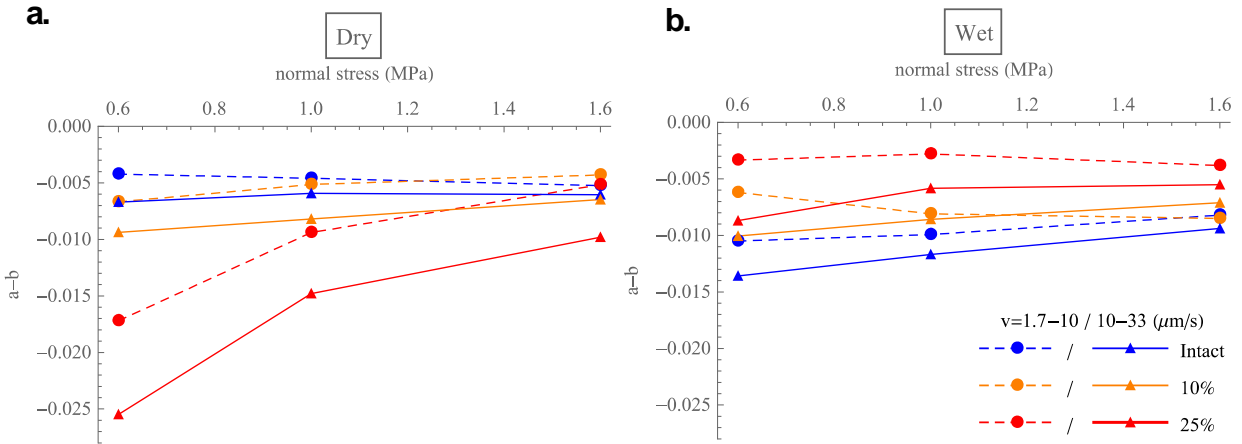
Figure 7. Effect of the normal stress on the rate and state friction parameters (a-b) plotted for the different velocity steps and for different rate of dissolution

3.2. Roughness of the grains

The dissolution of the calcite through contact with an acid solution before shearing affects not only the grain size distribution but also the shape of the particles. The shape and in particular the roughness of the grains could influence the mechanical response of the sample (Anthony and Marone 2005). Thus, we characterize the roughness and shape of the particles using the specific BET surface area (SA 3100 BET surface area and pore size analyzer; Beckman Coulter, U.S.), sieves analysis and a Scanning Electron Microscope (SEM).

The roughness of a given sample is defined as the ratio between the surface areas obtained from the BET method and the particle size analysis (considering spherical particles) as explained in (Micić et al. 2017). The BET method is a way to calculate the specific surface area of a sample based on gas adsorption. Nitrogen is pumped into the sample at a given pressure, with constant temperature (corresponding to the boiling point of liquid Nitrogen) and the adsorption process is measured volumetrically. The isotherm data obtained from this procedure enable to determine the specific surface area based on the theory developed by (Brunauer, Emmett, and Teller 1938) with an accuracy of 0.1 m^2/g. This value of the specific surface area can be compared with one obtained from the particle size distribution (PSD). The latter is obtained by assuming that the mass of material obtained for each size correspond to spherical particles with the diameter of the mesh size (or the size of the volume equivalent for laser diffraction). The results are reported in Table 4.

18

385

Sample	S_{PSD} (m^2/g)	S_{BET} (m^2/g)	Roughness
Intact	5.34×10^{-2}	0.96	18.03
10%	3.29×10^{-2}	0.83	25.32
25%	9.48×10^{-3}	0.99	104.32

386 *Table 4.Values of the specific surface area obtained from the BET method (SBET) or the particle size distribution (SPSD) and the*
387 *roughness for different level of dissolution*

388

389 The specific surface area obtained from the PSD exhibits a decrease with the amount of
390 dissolution. It is due to the more pronounced dissolution of the small particles that contributes
391 substantially to the value of the specific surface. However, the values obtained from the BET
392 method are not notably affected by the dissolution. Consequently, the roughness increases with
393 the increasing amount of dissolution. (Micić et al. 2017) have performed a similar methodology
394 to evaluate the roughness of different granular materials. They have observed a difference of
395 almost two orders of magnitude for the same definition of the roughness used here between glass
396 beads with a diameter of 1 mm and Dorsilit8 sand composed of 95% of quartz presenting
397 moderately well-sorted angular grains (0.3–0.8 mm), which shows that the difference of the
398 values of roughness reported in Table 4 are reasonable. To understand our results, observations
399 of the grains have been performed using a Variable Pressure Scanning Electron Microscope (FEI
400 XL30 SEM). The specimens have been coated with gold film prior to be placed in the
401 microscope. Images of the intact gouge and the gouge with 25% degradation are shown in Figure
402 8. The intact gouge exhibits much more fine particles attached to each other or to larger grains
403 than the samples which experienced dissolution. Moreover, grains with a diameter larger than 10
404 μm in the intact gouge (Figure 8. b) present an external surface that exhibits less asperities than
405 the one in the dissolved gouge (Figure 8. d).

406
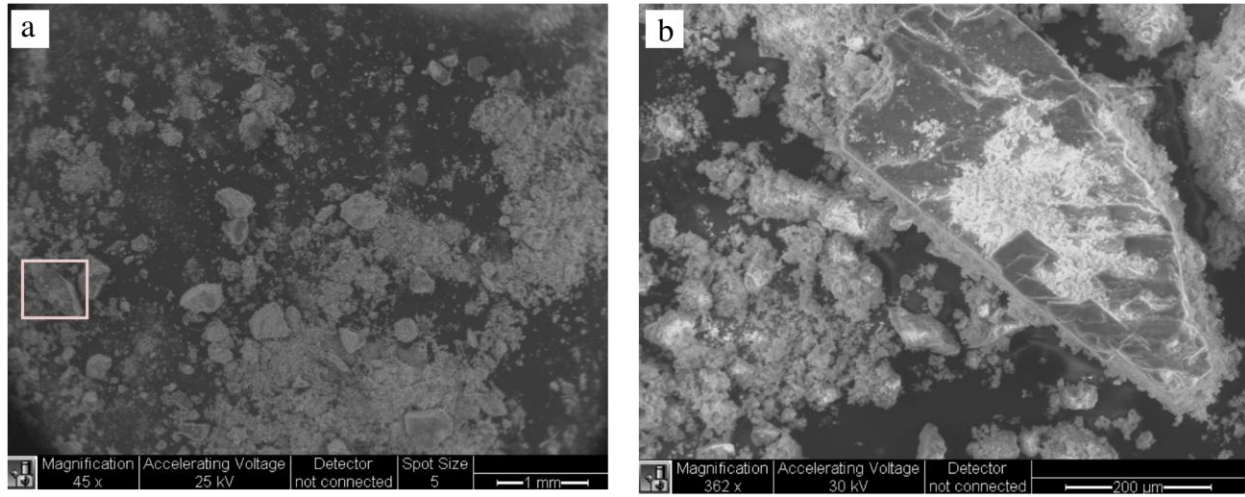
Intact sand

Dissolved sand 25%
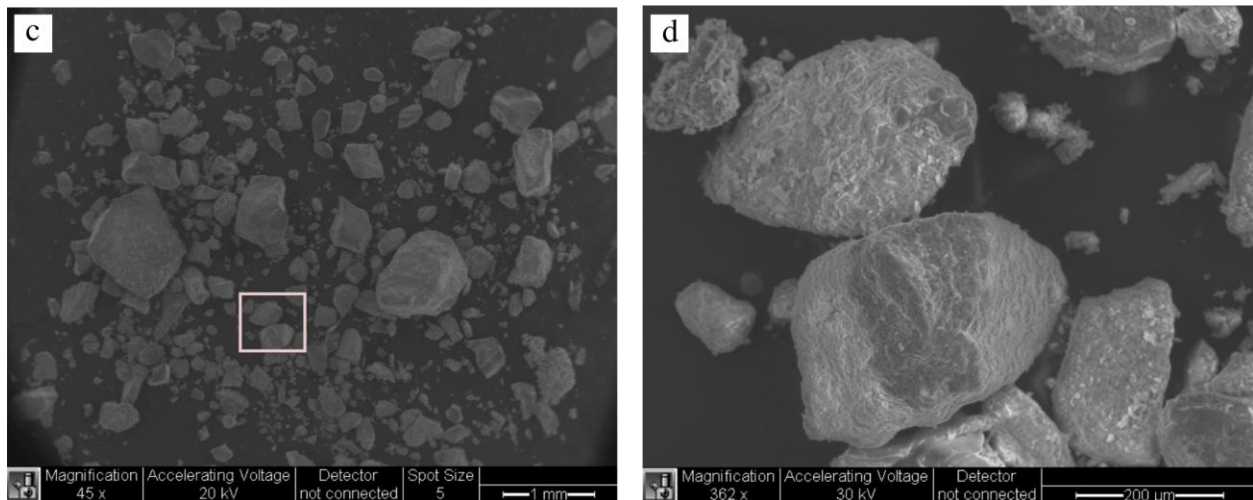
407

408 *Figure 8. Scanning Electron Microscope images of the intact gouge (a and b), and the gouge with 25% dissolution (c and d).*

409

410   **4. Discussion**

411   In this section, we integrate the mechanical data from our experiments and microstructural

412   investigation of the gouge prior to shear to discuss the role of the normal stress (see (A. M.H.

413   Pluymakers, Niemeijer, and Spiers 2016b) for a broader discussion on the effect of this

414   parameter), saturation of water and amount of dissolution on the velocity weakening behavior of

415   carbonate bearing faults. We also discuss the implications of our results in the context of

416   injection of an acidic fluid in a reservoir presenting faults composed of carbonates.

4.1. Comparison with other works

Our results show that the mechanical behavior of simulated carbonate-bearing faults is modulated by the imposed slip velocity, the normal stress, the amount of chemical dissolution of the grains and the presence of water inside the pores.

A number of experimental studies have focused on the frictional behavior of carbonate materials (Han et al. 2007; B. a. Verberne et al. 2013; Smith, Nielsen, and Di Toro 2015; Carpenter et al. 2016) under different range of temperature, velocities and normal stress using double direct shear and rotary shear experiments. They observed a strong resistance and a friction coefficient at the peak between 0.6 and 0.7, consistent with our observations for a normal stress of 600 kPa and sub-seismic velocities. The decrease of the peak friction coefficient in the presence of water has also been previously observed (B. a. Verberne et al. 2013), but the difference was less pronounced than in our observations for the dissolved samples. Moreover, the steady state friction coefficients obtained in experiments reported in the literature stay close to the peak value (at velocities below 1 cm/s), exhibiting thus almost no slip weakening or slip strengthening. This discrepancy is due to the size of the sample used in the ACSA as explained in (Guillaume Chambon, Schmittbuhl, and Corfdir 2006a). This macroscopic slip-weakening operating over centimetric distances is induced by a progressive mechanical decoupling between the interfacial layer and the bulk of the samples, as shown by image analysis during shearing (G. Chambon et al. 2003). This characteristic distance of the slip weakening is much larger than in previous experimental studies and fully consistent with values inferred for large earthquakes (Guillaume Chambon, Schmittbuhl, and Corfdir 2006b).

Experiments conducted on gouge at typical velocities consistent with earthquake nucleation (a few micrometers per seconds like here) exhibits velocity strengthening (B. A. Verberne et al. 2014) or a velocity neutral (Carpenter et al. 2016) for normal stresses below 20 MPa. The order of magnitude of the *(a-b)* coefficient, we have obtained (10^{-2}) is in agreement with previous studies on friction in gouge materials composed of quartz or carbonates (Biegel, Sammis, and Dieterich 1989; Carpenter et al. 2016). Nevertheless, our experiments reveal a velocity weakening behavior. This weakening has also been observed by (Guillaume Chambon 2003) for monodisperse quartz sand and glass beads using the annular shear apparatus. The difference in terms of *(a-b)* can be explained by the large displacements applied to the gouge in our

447 experiments before the velocity steps compared to experiments performed in double direct shear
448 or saw cut configurations. Large-displacement experiments using a rotary shear apparatus with
449 gouge samples have consistently shown a decrease of the friction rate parameter with
450 displacement and a transition from velocity-strengthening to velocity-weakening (Beeler et al.
451 1996; Marone 1998).

4.2. Micro-mechanisms affecting the rate and state friction parameters for dry experiments

454 For the range of normal stresses applied to our samples, the mechanical behavior of the dry
455 gouge is dominated by sliding and rotation of grains, the creation of force chains, cataclasis and
456 strain localization (Anthony and Marone 2005; Guillaume Chambon, Schmittbuhl, and Corfdir
457 2006a; B. a. Verberne et al. 2013). We focus in this section on the possible mechanisms driving
458 the experiments performed for the dry samples and compare with our observations to infer which
459 ones seem to dominate.

460 The dissolution of the calcite by an acid fluid before shearing affects the samples in two ways.
461 First, it generates a modification of the particle size distributions by dissolving preferably the
462 small grains. The fractal number of the distribution decreases and the mean grain size increases.
463 Moreover, the dissolution modifies the roughness of the particles. Both effects can influence the
464 frictional behavior of the sample.

465 (Anthony and Marone 2005) have studied the influence of particle roughness on the frictional
466 behavior of gouge using two materials: spherical glass beads and quartz sand, presenting
467 comparable particle size distributions. They have shown that an decrease of the
468 angularity/roughness of the grains for a similar grain size distribution tends to induce a
469 weakening of the apparent friction coefficient (Anthony and Marone 2005) and the triggering of
470 stick-slip instabilities (manifestation of a more negative rate and state parameter *(a-b)*).
471 However, our analysis of the roughness of the particles exhibits an increase with the dissolution
472 but a decrease of the apparent friction (see Figure 5 and Table 4) and a decrease of *(a-b)* towards
473 more negative values (Figure 6). Therefore, the decrease of the apparent friction and *(a-b)* with
474 the dissolution for dry experiments cannot be explained as a direct effect of the roughness of the
475 particles. In the present work, the particle size distribution changes (in addition to the roughness

476 of the grains) when subjected to dissolution, so this effect must dominate the mechanical
477 behavior of the sample and not the modification of the grains' roughness.

478 Compared to silica sand, carbonate sand presents a lower grain hardness and higher intraparticle
479 porosity, which makes them more susceptible to grain crushing (Coop et al. 2004). Recent papers
480 on granular mechanics have linked the rate dependency observed in sand to the crushing of
481 particles (Karimpour and Lade 2010; Y. D. Zhang and Buscarnera 2017; Das and Das 2019).
482 This effect induces a larger compaction rate and thus a stronger velocity-weakening behavior as
483 explained in (Marone 1998). For our experiments, the dissolution affects the width of the particle
484 size distribution and generates a narrower distribution and a higher fraction of large particle.
485 Therefore, the force chains between the grains can be expected to carry a higher load and to be
486 longer (Mair and Hazzard 2007; C. Ovalle et al. 2016). This can lead to a more important
487 comminution process, a decrease of friction and a larger velocity-weakening (a more negative *(a-*
488 *b)* parameter) as observed here for the dry experiments in Figure 9 and Figure 5. However, the
489 fact that we use multi-stage experiments and large displacements before applying the velocity
490 steps here induces that the velocity steps performed for lower normal stress are performed on a
491 material that is more subject to grain crushing and a larger compaction rate affecting the values
492 of *(a-b)* obtained.

493 In Figure 7 and Figure 9, the 25% dry experiments (and also less significantly the 10% dry) show
494 an increase of the *(a-b)* parameter with the normal stress. The other tests exhibit only a small
495 variation with the normal stress. This can be attributed to the fact that the experiments with 0.6
496 MPa normal stress are performed on the initial sample (not yet sheared) and the grains can be
497 more subject to grain crushing and thus a higher compaction rate, whereas the tests with higher
498 normal stresses are performed on samples that have already been sheared and thus, the
499 comminution has already modified the PSD.

a. velocity step 10-33 μm/s

b. velocity step 1.7-10 μm/s
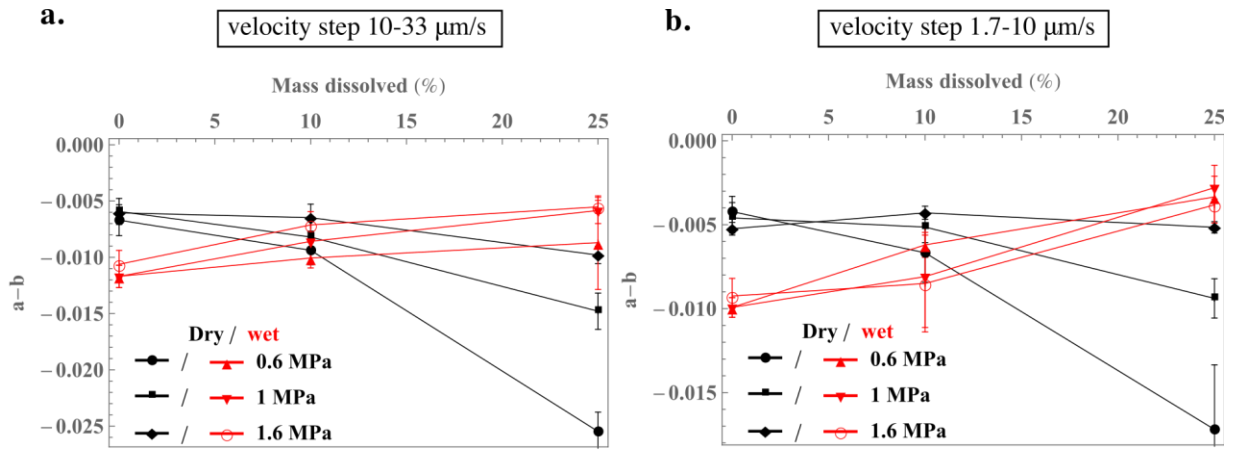
Figure 9. Comparisons of the average (a-b) parameter obtained for a given velocity jump as a function of the amount of dissolution for the wet and dry experiments. Error bars indicate the dispersion of the values of (a-b) between the different steps for the same values of the velocity.

Therefore, the mechanical behavior of the dry experiments is inferred to be mainly caused by the grain crushing that is more important for the dissolved samples as the particle size distributions become narrower as it allows to explain the evolution observed for the rate and state parameter *(a-b)* and the value of the friction coefficient.

4.3. Effects of water

In Figure 9, the values of *(a-b)* for a given step is represented as a function of the percentage of mass dissolved by the acid solution for different normal stresses and in presence or not of water. The different values obtained for a velocity step are calculated as an average of the values of the velocity jumps involving the same velocity values (velocity jump 10-33 μm/s: 1-2, 4-5, 5-6, 8-9; velocity jump 1.7-10 μm/s: 2-3, 3-4, 6-7, 7-8). We can observe that the presence of water modifies the influence of the dissolution on the coefficient (*a-b*). For dry experiments, the dissolution leads to more weakening of the rate parameters towards more negative values, whereas in the wet case it leads to an increase of the rate and state parameter *(a-b)*. Moreover, the addition of water modifies also the value of the friction coefficient at peak and steady state compared to the dry experiments (Figure 5). The peak friction is decreased by the presence of water compared to the dry experiments, however the steady state friction shows a larger value for the intact sample and a lower value in the wet tests compared to the dry tests.

As explained in (B. A. Verberne et al. 2014), the effect of unpressurized water is threefold regarding the frictional behavior of granular materials. Water can 1) promote compaction of the

24

523   specimen through pressure-solution; 2) lubricate grain contacts; or 3) stimulate cataclasis by

524   lowering the fracture toughness of the grains. The influence of these three mechanisms is

525   discussed in the following paragraphs and compared to our observations to infer which ones

526   dominate during the experiments presented here.

527   The phenomenon of pressure solution is a time-dependent chemo-mechanical process inducing a

528   compaction of rocks and granular assemblies when saturated. It is a dissolution-precipitation

529   mechanism in which the solid is dissolved in stressed regions and precipitates in sheltered

530   regions relatively under-stressed. This process is more active for fine grain materials (Niemeijer,

531   Elsworth, and Marone 2009), and would therefore tend to be more active in the intact gouge than

532   in the dissolved gouges in our case. (X. Zhang and Spiers 2005) performed creep experiments on

533   calcite with normal stresses between 1 and 4 MPa at room temperature and observed most of the

534   deformations induced by pressure solution happened within the first few hours of the

535   experiments. This timescale of pressure solution is similar to the total time of our tests for a

536   similar material and can therefore influence the mechanical behavior. In particular, pressure

537   solution during shearing at low velocities leads to a porosity reduction, an increasing grain

538   contact area (Bos, Peach, and Spiers 2000) and lower absolute value for (a-b) (more neutral)

539   (van den Ende et al. 2018). This phenomenon cannot explain the lower value of (a-b) for in the

540   wet case compared to the dry for the intact gouge as the slip distances between each velocity

541   jump is too small for it to develop. However, the increased gouge cohesion due to pressure-

542   solution in wet experiments should lead to a higher steady-state frictional strength than in dry

543   tests as observed in Table 3 for the intact and deg10 experiments, which are samples presenting

544   smaller grains than deg25 and are therefore more subject to pressure solution. It indicates that

545   this mechanism influences the value of the friction but not the rate and state parameter *(a-b)* in

546   our experiments.

547   The presence of water promotes grain breakage by decreasing the fracture toughness of

548   individual grains (Atkinson 1982; Carlos Ovalle et al. 2015; Y. Zhang and Buscarnera 2018).

549   This effect is usually referred as subcritical crack propagation and several theories have been

550   developed to explain it based on the modification of the plastic zone near the crack tip or

551   chemical interactions of the water with bonds at the crack tip (Y. Zhang and Buscarnera 2018).

552   This effect induces a larger compaction and thus a stronger velocity-weakening behavior. It can

553   explain the decrease of (a-b) for the intact gouge for the wet compared to the dry experiments

554   but not the results for the samples submitted to dissolution (in terms of difference wet versus
555   dry). Indeed, carbonate gouges can present a non-self-similar cataclasis and grain crushing is not
556   inhibited when reaching a fractal distribution with fractal number 2.6 and they can exhibit higher
557   fractal numbers than 2.6 (Storti, Billi, and Salvini 2003) compared to silica gouges. Also, the wet
558   intact sample is the only one of the wet experiments showing a small increase of (a-b) with the
559   normal stress, and therefore increasing displacements, for the two velocity steps (Figure 7),
560   which can also be an effect of the grain crushing as the compaction rate decreases with
561   increasing displacements. It should be noted that the effects of water like pressure solution or
562   grain crushing would affect the microstructure of the gouge and therefore the microstructure
563   would not be the same in the dry and wet samples after the initial shear of the material when the
564   velocity steps take place.

565   A third mechanism due to the presence of water is the intergranular lubrication, which decreases
566   intergranular friction and/or adhesion (Cornelio and Violay 2020). This phenomenon leads to a
567   decrease of friction coefficient and an evolution of (a-b) towards neutral velocity dependence in
568   the presence of water compared to the dry case as the effect of changing porosity and thus
569   contact area is less pronounced inducing in this way less velocity weakening (B. A. Verberne et
570   al. 2014). These two effects have been observed for the samples with 25% mass dissolution (see
571   Table 3 and Figure 9). The intergranular lubrication could be dominant in this case due to the
572   narrower particle size distribution and longer force chains becoming more unstable with the
573   lubrication. Moreover, it can explain the lower friction coefficient at peak for the wet samples
574   compared to the dry ones.

575   Therefore, the above considerations seem to indicate that the frictional behavior of our samples
576   in the presence of water appears to be more controlled by grain breakage/abrasion and pressure
577   solution (for the value of the friction coefficient at steady state) for the intact gouge, and to
578   intergranular lubrication for the degraded gouge (25%). The behavior of the gouge with 10%
579   dissolution is not much affected by the presence of water and it is probably a result of the
580   different mechanisms described above competing and counteracting each other. The importance
581   of these mechanisms is inferred to be a result of the narrower particle size distribution and not
582   the change of grains' roughness induced by dissolution. They lead to an increase of the rate and
583   state parameter (a-b) with dissolution for wet gouges, which would decrease the seismic
584   potential of a fault (that are most of the time saturated) by decreasing the critical stiffness under

585 which it is unstable (eq. 5). Nonetheless, this complex set of microphysical mechanisms
586 controlling frictional sliding in wet calcite gouges needs to be better constrained using
587 microphysical observations to evaluate the particle size distribution evolution at different stages
588 of the experiments and evidences of the mechanisms operating at the interface between the
589 grains. It will be the subject of future studies.

590 **4.4.Implications for fault reactivation**

591 Our results can have important implications for the study of CO_2 storage or acid gas injection
592 projects, but also to understand the mechanisms of carbonate bearing faults. Indeed, a great
593 number of earthquakes are triggered in such lithologies. Noteworthy examples of seismic slips
594 triggered and propagated through a fault composed of calcite are the magnitude 7.9 Wenchuan
595 (China) earthquake in 2008 (Chen et al. 2013), the magnitude 6.2 Aigion (Greece) earthquake in
596 1995 (Bernard et al. 1997), or the magnitude 7.6 Chi-Chi (China) earthquake in 1999 (Boullier et
597 al. 2009). Carbonate rocks are particularly ubiquitous in Italy and in the Apennines where the
598 tectonic activity produce number of seismic events, like in the Amatrice and Norcia areas for the
599 2016-17 seismic sequence (Pizzi et al. 2017), or in L'Aquila for the 2009 earthquake (Valoroso
600 et al. 2014). Moreover, many reservoirs in the world and potential sites for injection of CO2
601 storage or acid gas disposal are composed or carbonate materials (Bjorlykke 2010) and present
602 faults that may induce leakage from the storage if they would be reactivated.

603 Sliding along an existing fault favors grain comminution and abrasion and thus, an increase of
604 the fractal number (Storti, Billi, and Salvini 2003). Our results show that this increase of the
605 fractal number would tend to destabilize the gouge as faults in the crust are located in a wet
606 environment. On the other side, injection of an acid fluid tends to decrease this fractal number by
607 dissolving the small grains. This dissolution decreases the peak friction and promote reactivation
608 but also would reduce the velocity weakening of the fault and could prevent unstable (seismic)
609 slips.

610 In our experiments, the maximum amount of mass decrease due to dissolution of calcite that we
611 have considered is 25%. This high percentage of dissolved mass has been chosen to investigate
612 whether and how dissolution can affect the frictional properties of fault gouges and a lower
613 amount of dissolution would be expected in injection projects. However, (Bakker 2017) have
614 obtained a 25% decrease of calcite content for a carbonate gouge after 10,000 years of CO_2

615   injection based on geochemical simulations of the long term effect of CO_2 on the mineral
616   composition of a fault gouge, considering a residence time of 1000 years. In this study, the
617   authors considered a carbonate bearing claystone and have investigated the effect of long-term
618   exposure to CO_2 on the frictional properties of the fault by changing its mineral composition
619   according to the geochemical model and different scenarios. Therefore, the high percentages of
620   dissolution used in this study could potentially be reached after a long-term injection.

621   However, the experiments presented here have been performed at low normal stresses compared
622   to the stresses applied to faults at seismogenic depths or typical depths of potential CO_2 storage
623   sites, which are between at least 800 meters and 5 kilometers depth (Nakanishi et al. 2009), and
624   acid gas injection sites, which are between 700 meters and 5 kilometers depth (Bachu and Gunter
625   2002). This would result in normal stresses between 10 and 100 MPa at the fault and also higher
626   temperatures. The same mechanisms described above are expected to take place at the shallower
627   depths of the faults at these sites (below 50 MPa (Carpenter et al. 2016)), but their relative
628   importance would change. Pressure solution and grain crushing becomes both more important
629   with larger depths and they would have opposite effects on the rate and state parameter *(a-b)* (an
630   increase for pressure solution and a decrease for grain crushing). On the other side, the viscosity
631   of supercritical CO_2 is one tenth the one of water, which would affect grain lubrication and tend
632   to increase *(a-b)* (Cornelio and Violay 2020). At higher depths, crystal plastic deformation could
633   be triggered and would result in a semi-brittle behavior (Carpenter et al. 2016). Further
634   investigations would be required using an apparatus that allows to apply higher normal stresses
635   to the sample in order to further describe the influence of the different mechanisms at larger
636   depths.

637   **5. Concluding remarks**

638   In this paper, we investigate the effect of the injection of an acid fluid on the frictional properties
639   of a fault located in a carbonate reservoir. The rate and state parameter *(a-b)* of a simulated
640   calcite gouge are evaluated using an annular shear apparatus and conducting velocity stepping
641   experiments. The material is dissolved using a strong acid prior to mechanical tests in order to
642   investigate the potential effect of weak acids in the long-term. We observe that the long-term
643   exposure to an acid fluid can induce a decrease in the apparent friction and an increase in the rate
644   and state parameter *(a-b)* for a wet fault by dissolving the small particles and changing the fractal

number of the grain size distribution, whereas dry experiments exhibit a decrease of parameter (*a-b*) with dissolution. Our mechanical results are consistent with an interpretation that the frictional behavior of dry samples is controlled by grain breakage, which leads to a velocity weakening when the particles have been exposed to an acid. The presence of water induces different competing mechanisms: it promotes grain breakage and triggers pressure-solution and intergranular lubrication. Here, it is suggested that the dissolution of the grains causes a transition for the frictional behavior to be controlled by grain breakage and pressure-solution to a behavior more influenced by intergranular lubrication. However, the physical processes driving the shear behavior of the granular samples need to be further investigated and constrained from microstructural observations, which will be the focus of future studies. Finally, these experiments enable us to estimate that chemical reactions could potentially induce the reactivation of faults by modifying the grain size distribution and, thus, decreasing the apparent friction but also prevent seismic slip in a storage site by increasing the rate and state parameter (*a-b*) of the fault. However, this tendency needs to be confirmed by experiments performed with larger normal stress corresponding to the depths of injection.

References

Alevizos, S., Thomas Poulet, and Manolis Veveakis. 2014. "Thermo-Poro-Mechanics of Chemically Active Creeping Faults. 1: Theory and Steady State Considerations." *Journal of Geophysical Research: Solid Earth*, June, n/a-n/a. https://doi.org/10.1002/2013JB010070.

An, Lin Ji, and Charles G. Sammis. 1994. "Particle Size Distribution of Cataclastic Fault Materials from Southern California: A 3-D Study." *Pure and Applied Geophysics PAGEOPH* 143 (1–3): 203–27. https://doi.org/10.1007/BF00874329.

Anthony, Jennifer L., and Chris J. Marone. 2005. "Influence of Particle Characteristics on Granular Friction." *Journal of Geophysical Research B: Solid Earth* 110 (8): 1–14. https://doi.org/10.1029/2004JB003399.

676 Atkinson, Barry Kean. 1982. "Subcritical Crack Propagation in Rocks: Theory, Experimental
677   Results and Applications." *Journal of Structural Geology* 4 (1): 41–56.
678   https://doi.org/10.1016/0191-8141(82)90005-0.

679 Bachu, Stefan, and William D. Gunter. 2002. "Characteristics of Acid Gas Injection Operations
680   in Western Canada. Interim Report to International Energy Agency - Greenhous Gas R&D
681   Programme."

682 ———. 2004. "Acid-Gas Injection in the Alberta Basin, Canada: A C02-Storage Experience." In
683   *Geological Storage of Carbon Dioxid*, edited by R. H. BAINES, S. J. & WORDEN, 225–
684   34. Geological Society, London, Special Publications.

685 Baisch, Stefan, Robert Vörös, Elmar Rothert, Henrik Stang, Reinhard Jung, and Rüdiger
686   Schellschmidt. 2010. "A Numerical Model for Fluid Injection Induced Seismicity at Soultz-
687   Sous-Forets." *International Journal of Rock Mechanics and Mining Sciences* 47: 405–13.
688   https://doi.org/10.1016/j.ijrmms.2009.10.001.

689 Bakker, Elisenda. 2017. "Frictional and Transport Properties of Simulated Faults in CO2 Storage
690   Reservoirs and Clay-Rich Caprocks." *Utrecht Series in Earth Sciences №124*.

691 Beeler, N. M., T. E. Tullis, M. L. Blanpied, and J. D. Weeks. 1996. "Frictional Behavior of
692   Large Displacement Experimental Faults." *Journal of Geophysical Research B: Solid Earth*
693   101 (4): 8697–8715. https://doi.org/10.1029/96jb00411.

694 Bernard, P, P Briole, B Meyer, H Lyon-Caen, J-M Gomez, C Tiberi, C Berge, et al. 1997. "The
695   Ms=6.2, June 15, 1995 Aigion Earthquake (Greece): Evidence for Low Angle Normal
696   Faulting in the Corinth Rift." *Journal of Seismology* 1 (2): 131–50.

697 Biegel, Ronald L., Charles G. Sammis, and James H. Dieterich. 1989. "The Frictional Properties
698   of a Simulated Gouge Having a Fractal Particle Distribution." *Journal of Structural
699   Geology* 11 (7): 827–46. https://doi.org/10.1016/0191-8141(89)90101-6.

700 Billi, Andrea. 2005. "Grain Size Distribution and Thickness of Breccia and Gouge Zones from
701   Thin (<1 m) Strike-Slip Fault Cores in Limestone." *Journal of Structural Geology* 27 (10):
702   1823–37. https://doi.org/10.1016/j.jsg.2005.05.013.

703 Bjorlykke, Knut. 2010. *Petroleum Geoscience: From Sedimentary Enviroments to Rock Physics*.
704   *Petroleum Geoscience*. https://doi.org/10.1007/978-3-642-02332-3.

705 Blanpied, Michael L., David A. Lockner, and James D. Byerlee. 1995. "Frictional Slip of Granite
706   at Hydrothermal Conditions." *Journal of Geophysical Research* 100 (B7): 13045–64.
707   https://doi.org/10.1029/95JB00862.

708 Bos, B, C J Peach, and C J Spiers. 2000. "Frictional-Viscous Flow of Simulated Fault Gouge
709   Caused by the Combined Effects of Phyllosilicates and Pressure Solution." *Tectonophysics*
710   327: 173–74.

711 Boullier, Anne Marie, En Chao Yeh, Sébastien Boutareaud, Sheng Rong Song, and Chin Ho

Tsai. 2009. "Microscale Anatomy of the 1999 Chi-Chi Earthquake Fault Zone." *Geochemistry, Geophysics, Geosystems* 10 (3). https://doi.org/10.1029/2008GC002252.

Brunauer, Stephen, P. H. Emmett, and Edward Teller. 1938. "Adsorption of Gases in Multimolecular Layers." *Journal of the American Chemical Society* 60 (2): 309–19. https://doi.org/citeulike-article-id:4074706.

Cappa, Frederic. 2012. "Impact of CO2 Geological Sequestration on the Nucleation of Earthquakes." *Geophysical Research Letters, 38, L17313, 2011*, September. http://escholarship.org/uc/item/15f9x6mp#page-12.

Carpenter, B M, C Collettini, C Viti, and A Cavallo. 2016. "The Influence of Normal Stress and Sliding Velocity on the Frictional Behaviour of Calcite at Room Temperature: Insights from Laboratory Experiments and Microstructural Observations." *Geophysical Journal International* 205 (1): 548–61. https://doi.org/10.1093/gji/ggw038.

Chambon, G., J. Schmittbuhl, A. Corfdir, J. P. Vilotte, and S. Roux. 2003. "Shear with Comminution of a Granular Material: Microscopic Deformations Outside the Shear Band." *Physical Review E - Statistical Physics, Plasmas, Fluids, and Related Interdisciplinary Topics* 68 (1): 8. https://doi.org/10.1103/PhysRevE.68.011304.

Chambon, Guillaume. 2003. "Caractérisation Expérimentale Du Frottement Effectif Des Zones de Faille." École Nationale des Ponts et Chaussées. http://tel.archives-ouvertes.fr/tel-00006613/.

Chambon, Guillaume, Jean Schmittbuhl, and Alain Corfdir. 2006a. "Frictional Response of a Thick Gouge Sample: 1. Mechanical Measurements and Microstructures." *Journal of Geophysical Research: Solid Earth* 111 (9): 1–17. https://doi.org/10.1029/2003JB002731.

———. 2006b. "Frictional Response of a Thick Gouge Sample: 2. Friction Law and Implications for Faults." *Journal of Geophysical Research: Solid Earth* 111 (9): 1–12. https://doi.org/10.1029/2004JB003339.

Chen, Jianye, Xiaosong Yang, Shengli Ma, and Christopher J Spiers. 2013. "Mass Removal and Clay Mineral Dehydration/Rehydration in Carbonate-Rich Surface Exposures of the 2008 Wenchuan Earthquake Fault : Geochemical Evidence and Implications for Fault Zone Evolution and Coseismic Slip." *Journal of Geophysical Research : Solid Earth* 118 (2): 474–96. https://doi.org/10.1002/jgrb.50089.

Coop, M. R., K. K. Sorensen, T. Bodas Freitas, and G. Georgoutsos. 2004. "Particle Breakage during Shearing of a Carbonate Sand." *Geotechnique* 54 (3): 157–63. https://doi.org/10.1680/geot.2004.54.3.157.

Corfdir, Alain, Patrick Lerat, and Ioannis Vardoulakis. 2004. "A Cylinder Shear Apparatus." *Geotechnical Testing Journal* 27 (5): 447–55. https://doi.org/10.1520/gtj11551.

Cornelio, Chiara, and Marie Violay. 2020. "Effect of Fluid Viscosity on Earthquake Nucleation." *Geophysical Research Letters* 47: 1–9. https://doi.org/10.1029/2020GL087854.

749   Das, Soukat Kumar, and Arghya Das. 2019. "Influence of Quasi-Static Loading Rates on
750   Crushable Granular Materials: A DEM Analysis." *Powder Technology* 344 (January 2019):
751   393–403. https://doi.org/10.1016/j.powtec.2018.12.024.

752   Dieterich, James H. 1979. "Modeling of Rock Friction: 1. Experimental Results and Constitutive
753   Equations." *Journal of Geophysical Research* 84 (B5): 2161.
754   https://doi.org/10.1029/JB084iB05p02161.

755   ———. 1981. "Constitutive Properties of Faults with Simulated Gouge." *Geophysical*
756   *Monograph Series* 24: 103–20.
757   http://www.agu.org/books/gm/v024/GM024p0103/GM024p0103.shtml.

758   Ellsworth, William L. 2013. "Injection-Induced Earthquakes." *Science* 341 (July): 1–8.

759   Ende, M. P.A. van den, J. Chen, J. P. Ampuero, and A. R. Niemeijer. 2018. "A Comparison
760   between Rate-and-State Friction and Microphysical Models, Based on Numerical
761   Simulations of Fault Slip." *Tectonophysics* 733 (July 2017): 273–95.
762   https://doi.org/10.1016/j.tecto.2017.11.040.

763   Espinoza, D Nicolas. 2011. "Carbon Geological Storage – Underlying Phenomena and
764   Implications –."

765   Foulger, Gillian R, Miles P Wilson, Jon G Gluyas, Bruce R Julian, and Richard J Davies. 2018.
766   "Global Review of Human-Induced Earthquakes." *Earth-Science Reviews* 178 (July 2017):
767   438–514. https://doi.org/10.1016/j.earscirev.2017.07.008.

768   Han, Raehee, Toshihiko Shimamoto, T Hirose, J H Ree, and J Ando. 2007. "Ultralow Friction of
769   Carbonate Faults Caused by Thermal Decomposition." *Science* 316 (5826): 878–81.
770   https://doi.org/10.1126/science.1139763.

771   Karimpour, Hamid, and Poul V. Lade. 2010. "Time Effects Relate to Crushing in Sand." *Journal*
772   *of Geotechnical and Geoenvironmental Engineering* 136 (9): 1209–19.
773   https://doi.org/10.1061/(ASCE)GT.1943-5606.0000335.

774   Khan, Chawarwan, Robert Amin, and Gary Madden. 2013. "Effects of CO_2 and Acid Gas
775   Injection on Enhanced Gas Recovery and Storage." *Journal of Petroleum Exploration and*
776   *Production Technology* 3 (1): 55–60. https://doi.org/10.1007/s13202-012-0044-8.

777   Kirk-Othmer. 2004. *Kirk-Othmer Encyclopedia of Chemical Technology, Volume 4*. Edited by
778   Kirk-Othmer. 2004th ed. Hoboken, NJ: Wiley.

779   Koval, Georg, François Chevoir, Jean-Noël Roux, Jean Sulem, and Alain Corfdir. 2011.
780   "Interface Roughness Effect on Slow Cyclic Annular Shear of Granular Materials."
781   *Granular Matter* 13 (5): 525–40. https://doi.org/10.1007/s10035-011-0267-2.

782   Lund, Kasper, H. S. Fogler, C. C. McCune, and J. W. Ault. 1975. "Acidization-II. The
783   Dissolution of Calcite in Hydrochloric Acid." *Chemical Engineering Science* 30 (8): 825–
784   35. https://doi.org/10.1016/0009-2509(75)80047-9.

785   Mair, Karen, and James F. Hazzard. 2007. "Nature of Stress Accommodation in Sheared
786   Granular Material: Insights from 3D Numerical Modeling." *Earth and Planetary Science*
787   *Letters* 259 (3–4): 469–85. https://doi.org/10.1016/j.epsl.2007.05.006.

788   Marone, Chris J. 1998. "Laboratory-Derived Friction Laws and Their Application To Seismic
789   Faulting." *Annual Review of Earth and Planetary Sciences* 26 (1): 643–96.
790   https://doi.org/10.1146/annurev.earth.26.1.643.

791   Messen, Y. H., A. Corfdir, and J. Schmittbuhl. 2013. "Mechanical Healing of Simulated Fault
792   Gouge." *Geophysical Journal International* 193 (1): 252–62.
793   https://doi.org/10.1093/gji/ggs082.

794   Michael, K., A. Golab, V. Shulakova, J. Ennis-King, G. Allinson, S. Sharma, and T. Aiken.
795   2010. "Geological Storage of CO2 in Saline Aquifers-A Review of the Experience from
796   Existing Storage Operations." *International Journal of Greenhouse Gas Control* 4 (4): 659–
797   67. https://doi.org/10.1016/j.ijggc.2009.12.011.

798   Micić, Vesna, Doris Schmid, Nathan Bossa, Andreas Gondikas, Milica Velimirovic, Frank Von
799   Der Kammer, Mark R. Wiesner, and Thilo Hofmann. 2017. "Impact of Sodium Humate
800   Coating on Collector Surfaces on Deposition of Polymer-Coated Nanoiron Particles."
801   *Environmental Science and Technology* 51 (16): 9202–9.
802   https://doi.org/10.1021/acs.est.7b01224.

803   Mortezaei, Kimia, and Farshid Vahedifard. 2015. "Numerical Simulation of Induced Seismicity
804   in Carbon Capture and Storage Projects." *Geotechnical and Geological Engineering* 33 (2):
805   411–24. https://doi.org/10.1007/s10706-015-9859-7.

806   Nakanishi, Shigetaka, Yasunobu Mizuno, Tadahiko Okumura, Hideaki Miida, Takumi
807   Shidahara, and Shin-ichi Hiramatsu. 2009. "Methodology of CO2 Aquifer Storage Capacity
808   Assessment in Japan and Overview of the Project." *Energy Procedia* 1 (1): 2639–46.
809   https://doi.org/10.1016/j.egypro.2009.02.031.

810   Niemeijer, André, Derek Elsworth, and Chris Marone. 2009. "Significant Effect of Grain Size
811   Distribution on Compaction Rates in Granular Aggregates." *Earth and Planetary Science*
812   *Letters* 284 (3–4): 386–91. https://doi.org/10.1016/j.epsl.2009.04.041.

813   Ovalle, C., C. Voivret, C. Dano, and P.-Y. Hicher. 2016. "Population Balance in Confined
814   Comminution Using a Physically Based Probabilistic Approach for Polydisperse Granular
815   Materials." *International Journal for Numerical and Analytical Methods in Geomechanics*
816   40: 2383–2397. https://doi.org/10.1002/nag.

817   Ovalle, Carlos, Christophe Dano, Pierre Yves Hicher, and Mónica Cisternas. 2015.
818   "Experimental Framework for Evaluating the Mechanical Behavior of Dry and Wet
819   Crushable Granular Materials Based on the Particle Breakage Ratio." *Canadian*
820   *Geotechnical Journal* 52 (5): 587–98. https://doi.org/10.1139/cgj-2014-0079.

821   Pizzi, A., A. Di Domenica, F. Gallovic, L. Luzi, and R. Puglia. 2017. "Fault Segmentation as
822   Constraint to the Occurrence of the Main Shocks of the 2016 Central Italy Seismic

823   Sequence." *Tectonics* 36 (11): 2370–87. https://doi.org/10.1002/2017TC004652.

824   Pluymakers, A. M.H., A. R. Niemeijer, and C. J. Spiers. 2016a. "Frictional Properties of
825   Simulated Anhydrite-Dolomite Fault Gouge and Implications for Seismogenic Potential."
826   *Journal of Structural Geology* 84: 31–46. https://doi.org/10.1016/j.jsg.2015.11.008.

827   ———. 2016b. "Frictional Properties of Simulated Anhydrite-Dolomite Fault Gouge and
828   Implications for Seismogenic Potential." *Journal of Structural Geology*.
829   https://doi.org/10.1016/j.jsg.2015.11.008.

830   Pluymakers, Anne M H, Jon E Samuelson, André R Niemeijer, and Christopher J Spiers. 2014.
831   "Effects of Temperature and CO2 on the Frictional Behavior of Simulated Anhydrite Fault
832   Rock." *Journal of Geophysical Research : Solid Earth* 119,: 8728–8747.
833   https://doi.org/10.1002/2014JB011575.Received.

834   Rattez, Hadrien, Ioannis Stefanou, and Jean Sulem. 2018. "The Importance of Thermo-Hydro-
835   Mechanical Couplings and Microstructure to Strain Localization in 3D Continua with
836   Application to Seismic Faults. Part I: Theory and Linear Stability Analysis." *Journal of the
837   Mechanics and Physics of Solids* 115: 54–76. https://doi.org/10.1016/j.jmps.2018.03.004.

838   Rattez, Hadrien, Ioannis Stefanou, Jean Sulem, Manolis Veveakis, and Thomas Poulet. 2018.
839   "The Importance of Thermo-Hydro-Mechanical Couplings and Microstructure to Strain
840   Localization in 3D Continua with Application to Seismic Faults . Part II : Numerical
841   Implementation and Post-Bifurcation Analysis." *Journal of the Mechanics and Physics of
842   Solids* 115: 1–29. https://doi.org/10.1016/j.jmps.2018.03.003.

843   Rattez, Hadrien, Ioannis Stefanou, Manolis Veveakis, Thomas Poulet, and Jean Sulem. 2018.
844   "Numerical Analysis of Strain Localization in Rocks with THM Couplings: Benchmark
845   Tests and Microstructure." *Rock Mechanics and Rock Engineering*.

846   Rattez, Hadrien, Jean Sulem, and Siavash Ghabezloo. 2014. "Effect of CO2 on Fault Friction
847   and Slip Stability." In *25th ALERT Workshop, Aussois, France*.

848   Rattez, Hadrien, and Manolis Veveakis. 2020. "Weak Phases Production and Heat Generation
849   Control Fault Friction during Seismic Slip." *Nature Communications* 11 (350).
850   https://doi.org/10.1038/s41467-019-14252-5.

851   Reid, Harry F. 1910. "The Mechanism of the Earthquake." In *The California Earthquake of April
852   18, 1906, Report of the State Earthquake Investigation Commision, Vol. 2*, 1–192.

853   Rice, James R. 2006. "Heating and Weakening of Faults during Earthquake Slip." *Journal of
854   Geophysical Research: Solid Earth* 111 (5). https://doi.org/10.1029/2005JB004006.

855   Rice, James R., and A Ruina. 1983. "Stability of Steady Frictional Slipping." *Journal of Applied
856   Mechanics* 50 (2): 343. https://doi.org/10.1115/1.3167042.

857   Rohmer, J., A. Pluymakers, and F. Renard. 2016. "Mechano-Chemical Interactions in
858   Sedimentary Rocks in the Context of CO2 Storage: Weak Acid, Weak Effects?" *Earth-*

859   *Science Reviews* 157 (June 2016): 86–110. https://doi.org/10.1016/j.earscirev.2016.03.009.

860   Rubinstein, Justin L., and Alireza Babaie Mahani. 2015. "Myths and Facts on Wastewater
861   Injection, Hydraulic Fracturing, Enhanced Oil Recovery, and Induced Seismicity."
862   *Seismological Research Letters* 86 (4): 1060–67. https://doi.org/10.1785/0220150067.

863   Ruina, A. 1983. "Slip Instability and State Variable Friction Laws." *Journal of Geophysical*
864   *Research: Solid   Earth*   88   (12):   10,359-10,370.
865   http://onlinelibrary.wiley.com/doi/10.1029/JB088iB12p10359/full.

866   Sammis, Charles G., Geoffrey King, and Ronald L. Biegel. 1987. "The Kinematics of Gouge
867   Deformation."   *Pure   and   Applied   Geophysics*   125   (5):   777–812.
868   https://doi.org/10.1007/BF00878033.

869   Samuelson, Jon E, and Christopher J Spiers. 2012. "Fault Friction and Slip Stability Not
870   Affected by CO2 Storage : Evidence from Short-Term Laboratory Experiments on North
871   Sea Reservoir Sandstones and Caprocks." *International Journal of Greenhouse Gas Control*
872   Volume 11 (November 2012): 78–90.

873   Schoenball, Martin, and William Ellsworth. 2017. "A Systematic Assessment of the
874   Spatiotemporal Evolution of Fault Activation Through Induced Seismicity in Oklahoma and
875   Southern Kansas." *Journal of Geophysical Research : Solid Earth* 122 (12): 10,189-10,206.
876   https://doi.org/10.1002/2017JB014850.

877   Scholz, Christopher H. 1998. "Earthquakes and Friction Laws." *Nature* 391 (January 1998): 37–
878   42.

879   Scuderi, Marco M., André R Niemeijer, Cristiano Collettini, and Chris J. Marone. 2013.
880   "Frictional Properties and Slip Stability of Active Faults within Carbonate–Evaporite
881   Sequences: The Role of Dolomite and Anhydrite." *Earth and Planetary Science Letters*
882   369–370 (May): 220–32. https://doi.org/10.1016/j.epsl.2013.03.024.

883   Smith, Steven A. F., Stefan Nielsen, and Giulio Di Toro. 2015. "Strain Localization and the
884   Onset of Dynamic Weakening in Calcite Fault Gouge." *Earth and Planetary Science Letters*
885   413 (March): 25–36. https://doi.org/10.1016/j.epsl.2014.12.043.

886   Steacy, S J, and C G Sammis. 1991. "An Automaton for Fractal Patterns of Fragmentation."
887   *Nature* 353 (6341): 250–52. https://doi.org/10.1038/353250a0.

888   Storti, Fabrizio, Andrea Billi, and Francesco Salvini. 2003. "Particle Size Distributions in
889   Natural Carbonate Fault Rocks : Insights for Non-Self-Similar Cataclasis." *Earth and*
890   *Planetary Science Letters* 206: 173–86.

891   Sulem, Jean, and V Famin. 2009. "Thermal Decomposition of Carbonates in Fault Zones: Slip-
892   Weakening and Temperature-Limiting Effects." *Journal of Geophysical Research* 114 (B3):
893   1–14. https://doi.org/10.1029/2008JB006004.

894   Tembe, Sheryl, David A. Lockner, and Teng Fong Wong. 2010. "Effect of Clay Content and

895   Mineralogy on Frictional Sliding Behavior of Simulated Gouges: Binary and Ternary
896   Mixtures of Quartz, Illite, and Montmorillonite." *Journal of Geophysical Research: Solid*
897   *Earth* 115 (3): 1–22. https://doi.org/10.1029/2009JB006383.

898 Torabi, A., M. U. Johannessen, and T. S. S. Ellingsen. 2019. "Fault Core Thickness: Insights
899   from Siliciclastic and Carbonate Rocks." *Geofluids* 2019: 1–24.
900   https://doi.org/10.1155/2019/2918673.

901 Unterreiner, P., P. Lerat, I. Vardoulakis, F. Schlosser, E. De Laure, and G. Belmont. 1993.
902   Brevet sur l'Appareil de Cisaillement Simple Annulaire (ACSA), issued 1993.

903 Valoroso, Luisa, Lauro Chiaraluce, Cristiano Collettini, Istituto Nazionale, Vigna Murata,
904   Dipartimento Scienze, Sapienza Università, and Piazzale Aldo Moro. 2014. "Earthquakes
905   and Fault Zone Structure." *Geology* 42 (4): 343–46. https://doi.org/10.1130/G35071.1.

906 Verberne, B. a., Christopher J Spiers, a. R. Niemeijer, J. H. P. Bresser, D. a. M. Winter, and O.
907   Plümper. 2013. "Frictional Properties and Microstructure of Calcite-Rich Fault Gouges
908   Sheared at Sub-Seismic Sliding Velocities." *Pure and Applied Geophysics*, December.
909   https://doi.org/10.1007/s00024-013-0760-0.

910 Verberne, B. A., Christopher J Spiers, André R Niemeijer, J. H P De Bresser, D. A M De Winter,
911   and O. Plümper. 2014. "Frictional Properties and Microstructure of Calcite-Rich Fault
912   Gouges Sheared at Sub-Seismic Sliding Velocities." *Pure and Applied Geophysics* 171
913   (10): 2617–40. https://doi.org/10.1007/s00024-013-0760-0.

914 Verberne, Berend A., André R. Niemeijer, Johannes H.P. De Bresser, and Christopher J. Spiers.
915   2015. "Mechanical Behavior and Microstructure of Simulated Calcite Fault Gouge Sheared
916   at 20–600°C: Implications for Natural Faults in Limestones." *Journal of Geophysical*
917   *Research: Solid Earth* 120: 8169–96. https://doi.org/10.1002/2015JB012292.Received.

918 Veveakis, Manolis, Thomas Poulet, and S. Alevizos. 2014. "Thermo-Poro-Mechanics of
919   Chemically Active Creeping Faults: 2. Transient Considerations." *Journal of Geophysical*
920   *Research: Solid Earth* 119 (6): 4583–4605. https://doi.org/10.1002/2013JB010071.

921 Wilson, M. P., G. R. Foulger, J. G. Gluyas, R. J. Davies, and B. R. Julian. 2017. "*HiQuake*: The
922   Human- Induced Earthquake Database." *Seismological Research Letters* 88 (6): 1560–65.
923   https://doi.org/10.1785/0220170112.

924 Yehya, Alissar, Zhuo Yang, and James Robert Rice. 2018. "Effect of Fault Architecture and
925   Permeability Evolution on Response to Fluid Injection." *Journal of Geophysical Research:*
926   *Solid Earth* 123 (11): 9982–97. https://doi.org/10.1029/2018JB016550.

927 Zhang, X., and C. J. Spiers. 2005. "Compaction of Granular Calcite by Pressure Solution at
928   Room Temperature and Effects of Pore Fluid Chemistry." *International Journal of Rock*
929   *Mechanics and Mining Sciences* 42: 950–60. https://doi.org/10.1016/j.ijrmms.2005.05.017.

930 Zhang, Y. D., and G. Buscarnera. 2017. "A Rate-Dependent Breakage Model Based on the
931   Kinetics of Crack Growth at the Grain Scale." *Géotechnique* 67 (11): 953–67.

932   https://doi.org/10.1680/jgeot.16.p.181.

933   Zhang, Yida, and Giuseppe Buscarnera. 2018. "Breakage Mechanics for Granular Materials in
934   Surface-Reactive Environments." *Journal of the Mechanics and Physics of Solids* 112: 89–
935   108. https://doi.org/10.1016/j.jmps.2017.11.008.

936